A Mission Profile Based Reliability Modeling Framework for Fault-tolerant Electric Propulsion

Alastair P. Thurlbeck, *Student Member, IEEE,* and Yue Cao, *Member, IEEE*

***Abstract*—This paper proposes a thermally-enhanced reliability modeling framework which works from the mission profile of an electrified aviation propulsion system, incorporating known fault-tolerant power electronics, motor drives, control, and their pre- and post-fault behaviours. The reliability framework is presented in a hierarchical fashion. Multiphysics modeling is used, incorporating electromechanical states, power losses, and thermal behaviors. The approach includes the device thermal stress in healthy and post-fault operating states in the failure rate calculations. Markov chain models are then used with the calculated failure rates to form system level reliability models. A case study of an electric vertical takeoff and landing urban aerial vehicle (eVTOL UAV) walks through the proposed method, modeling multiple versions of the propulsion system, with various levels of fault tolerance and redundancy. The proposed reliability modeling framework captures the operating temperatures and thermal swings seen by the components due to the flight mission, enhancing the failure rate calculation. Further, since the post-fault operating mode of the fault tolerant system causes higher component currents and temperatures, different component failure rates are calculated for post-fault operation. Finally, the Markov chain modeling allows for a reliability comparison between various UAV propulsion systems, including the effect of combining fault tolerance at the subsystem level, with redundancy at the system level.**

***Index Terms*—Fault-tolerance, redundancy, reliability modeling, PMSM drives, DC-AC inverters, aviation electrification, eVTOL UAV.**

I. Introduction

A. Background

Fault tolerance is frequently used to improve the reliability of mission-critical power electronic systems. For example, AC motors driven by DC-AC inverters have found many applications in electrified aircraft: actuating the flight control surfaces via an electro-hydraulic-actuator [2]–[4]; hybrid propulsion systems [5]; and all-electric propulsion systems where the electric motor is the sole propulsion force [6]. Without fault tolerance or redundancy, the entire system is vulnerable to catastrophic failure should a failure occur within the power-electronic system. Fault tolerance enables the system to continue operating despite a failure occurrence. Compared to a fully redundant system, fault tolerance offers limited redundancy, but with the advantage of relatively small increases in system cost, volume, and mass. However, performance in the post-fault state may be reduced compared to the healthy state, and the fault-tolerant system may retain some single points of failure. Therefore, fault tolerance by itself may not be a replacement for fully redundant systems, though can still improve reliability.

That said, adding fault-tolerant features does not necessarily improve system reliability due to the introduced complexity. Therefore, it is useful to quantify the change in reliability due to fault tolerance through reliability modeling. Beyond comparing the relative reliability of fault-tolerant systems, modeling can determine if the system reliability specification is met. The calculation of component failure rates is typically based on either an empirical approach using historical failure data or an analytical physics-of-failure (PoF) method [7]–[9]. In the former case, some commonly used datasets and methods are MIL-HDBK-217 [10], IEC 62380 [11] (formerly RDF 2000), and FIDES [12]. The empirical approaches allow for straightforward failure rate calculation, and IEC 62380 and FIDES can incorporate device thermal behaviours. In the latter case, however, PoF offers greater accuracy since the failure rate calculation is based on the actual physics of the failure modes in each component.

Since component degradation and aging depends on thermal stresses, a reliability modeling approach which considers the system's mission profile is necessary. In an inactive state, components are subjected to daily thermal cycles due to the natural ambient temperature variation of their operating environment. In operation, all components observe an on/off thermal cycle as the PCB and air are heated by conduction losses. In the power-electronic circuit, components which conduct the load current, such as the MOSFETs in an inverter, may see multiple large changes in device junction temperature over the course of the mission. Since most of the thermal stress is caused by the loading conditions, failure rate calculation is enhanced by considering the system mission profile.

B. Related Work

Researchers have previously presented mission profile based reliability methods using PoF analysis [13], [14]. However, the PoF method requires detailed theoretical analysis of each component's various failure modes. In the preliminary design stage of a power-electronic system, it is useful to have a concise, well defined framework with which to compare the relative reliability of a fault-tolerant system to a baseline system without fault tolerance, or to consider reliability in a down-selection from multiple system options. In this context, methods based on empirical data can be used to enable rapid

This work was supported in part by the Oregon State University Foundation and in part by the U.S. Department of Energy Advanced Research Projects Agency-Energy (ARPA-E) Award under Grant DE-AR0001438.

Preliminary work of this paper was presented (oral session) at the 2020 IEEE Energy Conversion Congress & Expo (ECCE), Detroit, Michigan, USA [1].

A. P. Thurlbeck and Y. Cao are with the School of Electrical Engineering and Computer Science, Oregon State University, Corvallis, OR 97331, USA. e-mail: thurlbea@oregonstate.edu, yue.cao@oregonstate.edu.

TABLE I
COMPARISON OF RELIABILITY MODELING APPROACHES

Method	Reliability Modeling Methods	Mission Profile Based?	Loss Calculation and Thermal Modeling	Thermal Cycle Extraction Method	Reliability Measures
[13]	PoF analysis using Coffin-Manson equation and Palmgren - Miner linear cumulative damage model	Yes	Multi-domain simulation including power loss and thermal modeling	Rainflow counting algorithm	Lifetime prediction
[14]	PoF analysis using Coffin-Manson equation and Palmgren-Miner linear cumulative damage model	Yes	Electrothermal model created from experimental loss measurements	Real-time rainflow counting algorithm	Real-time life consumption estimation
[15]	MIL-217; RDF 2000 (predecessor to IEC 62380); PoF analysis using Coffin-Manson and Arrhenius equations	Yes	Power loss estimated using datasheet method; lumped parameter thermal model	Evaluation of local maxima and minima	Reliability prediction calculated as MTTF* and lifetime prediction
[16]–[18]	Empirical data, including MIL-217; Markov chains	No	No	N/A	Reliability prediction of fault-tolerant drives based on R(t)* or MTTF*
[19]	Empirical data (source undefined); Markov chains; fixed 'normal' and 'stressed' failure rates	No	No	N/A	Reliability prediction of fault-tolerant drives based on MTTF*
Proposed	Empirical data using IEC 62380; Markov chains; failure rates calculated for each state according to thermal cycling	Yes	Multiphysics simulation, power loss from device level SPICE models; lumped parameter thermal model	Evaluation of local maxima and minima (modified method from [15])	Reliability prediction of fault-tolerant and redundant systems based on MTTF*, MTBF*, MTBR*

*Defined in Section II.

reliability prediction of the systems under study at the expense of absolute accuracy. Indeed, [15] details mission profile based failure rate calculations using both MIL-217 and IEC 62380, including device thermal behavior in the IEC 62380 method. However, device losses are calculated from datasheet parameters, as opposed to a transient switching simulation or experimental data. Further, the application of these mission profile based techniques to fault-tolerant or redundant systems is not demonstrated.

On the other hand, there are numerous reliability studies of fault-tolerant systems which use Markov chain modeling to compare between multiple fault-tolerant topologies or to a baseline system [16]–[20]. However, these existing studies do not consider the system mission profile. Instead, failure rates are based on empirical data or previously reported data, without consideration of device thermal cycles or operating temperatures. Further, of the aforementioned studies, only [19] uses altered component failure rates in the post-fault state, and even then the "normal" and "stressed" failure rates are generic predefined values.

C. Major Contributions

This paper aims to bridge the gap between mission profile based reliability modeling and the reliability analysis of fault-tolerant systems. We propose a thermally enhanced reliability modeling framework for the reliability prediction of fault-tolerant or redundant power electronic systems. Whilst the failure rates still originate from empirical data, failure rate calculations within IEC 62380 incorporate thermal behaviors via Arrhenius and Coffin-Manson based acceleration factors. Therefore, the proposed framework leverages multiphysics simulation and a thermal cycle extraction algorithm to provide the required temperature data. This represents a significant improvement over the existing fault-tolerant system reliability studies which do not consider the device temperature variations due to the load and fault-tolerant control method when obtaining failure rates. Losses are determined using transient simulation of device level SPICE models, which are then incorporated into the system level multiphysics simulation using three dimensional lookup tables. A lumped parameter thermal model then yields device junction temperatures over the system's mission profile. Finally, Markov chain models are used to determine system reliability rates and produce quantifiable reliability metrics. This approach is especially useful for evaluating the reliability of a fault-tolerant or redundant system, since failure rates are recalculated for any additional operating states in which device thermal behaviors deviate from healthy operation. Since the failure rate calculation utilizes IEC 62380, detailed knowledge of device failure mechanisms is not required. Thus the proposed framework enables rapid reliability comparisons between multiple system options, whilst still considering the reliability impact of thermal behaviors and fault-tolerant or redundant system design.

Table I compares the proposed framework to the existing approaches. Similar to [13]–[15], the proposed method estimates reliability by considering the system's mission profile, device losses, and device thermal behaviors including thermal cycling. Whilst [13], [14] use the PoF technique, the proposed framework calculates modified failure rates using the IEC 62380 standard according to Arrhenius and Coffin-Manson acceleration factors for the die and package receptively. Therefore, although failure rates are based on empirical data, they are modified using similar relations to those applied in a PoF analysis, and the proposed framework is designed to generate the required temperature and thermal cycle data according to the system's mission profile. The inclusion of thermal behaviors via these physics-based acceleration factors in the IEC 62380 failure rate calculations offers a distinct

This article has been accepted for publication in a future issue of this journal, but has not been fully edited. Content may change prior to final publication. Citation information: DOI 10.1109/TIA.2022.3144620, IEEE Transactions on Industry Applications

advantage over the purely empirical approaches in [16]–[19]. Compared to [15] which calculates device losses from the datasheet parameters, in this work losses are calculated from transient simulations of the turn-on and turn-off switching behaviors using device SPICE models. Whilst this method may be slightly less accurate than the experimental approach used by [14], the simulation based method better supports rapid application of the framework during the system design phase. Similar to [15], this work identifies thermal cycles by evaluating the local maxima and minima of a temperature profile, which yields similar results to a rainflow counting algorithm without any half-cycles.

The proposed framework is advantageous for comparing the relative reliability of fault-tolerant or redundant system designs. Since the framework uses the IEC 62380 standard, only easily obtainable component specifications are required for the computation of failure rates. Although a comprehensive PoF analysis is expected to be the most accurate approach for the reliability prediction of a single system, for comparison of multiple systems or of fault-tolerant or redundant designs, the proposed framework is far easier to implement and does not require any experimental data.

Beyond providing a detailed simulation method for mission-profile based failure rate calculation, the framework allows full consideration of fault-tolerant behaviors on reliability. Firstly, the system mission profile may be altered for post-fault operation. Secondly, even if the system mission profile is unchanged, the operating conditions seen by individual devices may be different in the post-fault operating mode. For example, if a 4th inverter leg connected to the motor neutral is used to add fault tolerance to a three-phase motor drive [21], the post-fault operating state requires $\sqrt{3}$ times current through the remaining two phase legs for the same load condition at the motor. If a component is subjected to increased thermal stresses in the post-fault operating state, this is reflected in increased thermal cycles. Therefore, a component's failure rate may change from healthy to post-fault operation.

D. Paper Organization

The paper is structured as follows. Section II details the proposed mission profile based reliability modeling framework for fault-tolerant systems. In Sections III and IV, a case study of an eVTOL UAV propulsion system using a 4th leg to neutral fault-tolerant strategy is used to demonstrate the proposed framework. Section III describes the studied fault-tolerant or redundant system versions, the selected fault-tolerant technique, and the system parameters and mission profile. Then in Section IV, the eVTOL UAV inverter and propulsion systems are used to walk through the reliability modeling framework in a concrete manner. Finally, Section V concludes the paper by considering the relevance and impact of the proposed framework.

II. Mission Profile based Reliability Modeling Framework

The proposed reliability modeling framework uses a five-step process as shown in Fig. 1. In Step 1, a multiphysics simulation approach obtains semiconductor device temperatures over the system mission profile. With regard to fault-tolerant systems, additional simulations are performed for any post-fault operating modes, considering the post-fault reconfiguration and control of the power-electronic system. In Step 2, the simulated temperature profiles are passed to a MATLAB algorithm, which automatically extracts the thermal cycle information. In Step 3, the thermal cycles are included in component failure rate calculations using IEC 62380. In Step 4, Markov chain models form reliability models of each system under study. Additional Markov states capture the effect of fault-tolerant or redundant systems, and Markov transition rates are calculated with consideration of any fault-tolerant circuitry or state-dependent component failure rates. Finally, Step 5 details the calculation of reliability metrics, including Mean Time To Failure (MTTF), or Mean Time Between Failures (MTBF) and Mean Time Between Repairs (MTBR) for fault-tolerant or redundant systems. The following subsections describe each step in a generic manner, while a detailed case study example is presented in Sections III and IV.

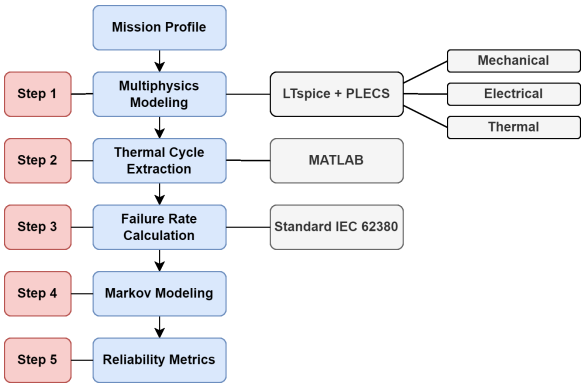

Fig. 1. Overview of the mission profile based reliability modeling framework.

A. Step 1: Multiphysics Modeling

The first step of the process obtains MOSFET junction temperatures over the given mission profile. In this paper, PLECS software is used, though a similar approach can be used in MATLAB/Simulink. The PLECS model includes mechanical, electrical, and thermal systems, as well as the system controls. Therefore, PLECS is used to perform a system-level dynamic simulation, with the aim of determining the semiconductor device temperatures over the entire mission profile. The system must be simulated for each of the possible missions or operational states. For example, a fault-tolerant system may have one or more post-fault operating states in which the device thermal behaviors are different.

In PLECS the switching devices are ideal and the transient switching behaviour is not simulated. Instead, 3-D lookup tables are used to obtain MOSFET conduction and switching losses according to the device temperature, voltage, and current at turn-on and turn-off. Simulation in LTspice generates the required lookup table data by using the semiconductor device manufacturer's SPICE model in double-pulse tests.

This article has been accepted for publication in a future issue of this journal, but has not been fully edited. Content may change prior to final publication. Citation information: DOI 10.1109/TIA.2022.3144620, IEEE Transactions on Industry Applications

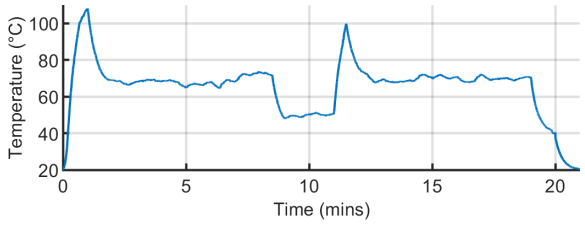

Fig. 2. Temperature profile used for thermal cycle extraction method comparison in Table II.

TABLE II
EXAMPLE DATA SHOWING DIFFERENCES AMONG THERMAL CYCLE EXTRACTION METHODS

Method	Extracted Thermal Cycles over Mission Profile ($^\circ C$)						
Rainflow	88.1*	3.35	3.37	9.34	51.7	4.96	4.55
[15]	88.1	3.35	3.37	9.34	32.3	4.55	4.65
Proposed	88.1	3.35	3.37	9.34	51.7	4.86	4.65

*The rainflow method identifies two half-cycles of $88.1^\circ C$.

Decoupling the switching device turn-on and turn-off transient behavior from the system-level simulation in PLECS is intentional and highly beneficial. The system-level PLECS model is simulated over the entire mission profile, and a time-step of the order of microseconds yields a reasonable simulation time whilst still including pulse-width-modulation (PWM) switching, controls, and dynamic system behavior. However, simulating switching device turn-on and turn-off behavior requires a time-step of the order of nano or picoseconds. Therefore, double-pulse testing in LTspice captures this behavior over a large number of discrete operating points. Then the system-level PLECS simulation interpolates switching turn-on and turn-off energies and device on-state voltages from the LTspice data lookup tables. This allows efficient and accurate simulation of semiconductor device losses and thermal behaviors over the system mission profile.

If a SPICE model is not available for the chosen device, experimental loss data or loss calculation from datasheet parameters [22] can be used instead. However, whilst the experimental data offers improved accuracy it is time consuming to collect, and whilst calculating losses from datasheet parameters is straightforward, the accuracy is often questionable.

B. Step 2: Thermal Cycle Extraction

In IEC 62380, the MOSFET package's base failure rate is modified with a Coffin-Manson derived acceleration factor, which uses the number (frequency) and magnitude of all thermal cycles experienced over a year. A MATLAB algorithm extracts thermal cycles from the thermal simulation results obtained in the previous step, where a thermal cycle is a corresponding rise and fall in temperature. The algorithm first identifies all the local maxima and minima corresponding to temperature changes greater than 3°C, as detailed in [15]. The cycles are then extracted from the maxima and minima according to the following steps: 1) the main thermal cycle is calculated as the global maximum minus the mean of the beginning and ending minima; 2) the subcycles are found as each maximum minus the immediate neighboring minimum closest in time to the global maximum. Identifying the subcycles this way ensures all maxima and minima are used once. This method is similar to the cycle extraction steps suggested in [15]; however, [15] finds subcycles as each remaining maximum minus its highest neighboring minimum, thereby ignoring outlying dips in the temperature profile unless they are manually identified.

The MATLAB function detailing the above steps is included in the Appendix. The function inputs are vectors of the identified maxima and minima with lengths n and n+1 respectively, and the function outputs a vector of the extracted cycle magnitudes. This MATLAB function is nested within a parent function which identifies all the maxima and minima from an input temperature profile. The parent function is not included here since its behavior does not deviate from [15]. Additionally, readers may utilize built-in MATLAB functions for this task.

Table II compares the modified method used here in this paper to that in [15] and also the rainflow counting method as defined in [23], all processed under the common temperature profile shown in Fig. 2. The motivation behind the method of [15] is to avoid the half-cycles output by the rainflow method. However, the suggested method in [15] neglects some of the dips in calculating cycle magnitudes, whilst the proposed modified algorithm fixes this issue.

C. Step 3: Failure Rate Calculation

Although failure rates in IEC 62380 are calculated based on empirical data, the calculations incorporate acceleration factors using the Arrhenius and Coffin-Manson models, as well as stress and environmental factors. For example, in the failure rate calculation for MOSFETs, the base failure rate of the device's die is multiplied by a charge factor for voltage stress and an Arrhenius acceleration factor, which considers device junction temperatures in each phase of the mission profile. The Arrhenius relation has an activation energy of 0.3 eV and a test temperature of 100°C. The acceleration factors for each phase are combined by weighting for the time spent in each phase. Similarly, the base failure rate of the semiconductor package is multiplied by an acceleration factor based on a modified Coffin-Manson model, which considers the number of thermal cycles and their respective magnitudes. The final failure rate is a summation of the modified die and package failure rates as well as an additional component for electrical overstress.

Using the thermal cycles from the previous step, as well as the average junction temperature of the MOSFETs observed in Step 1, a "thermal mission profile" is constructed for the MOSFETs. Note that this "thermal mission profile" is defined within IEC 62380 and is distinct from the system's mission profile used in Steps 1 and 2. It details all the thermal cycles and average operating temperatures endured by the component over an entire year. Therefore, environmental temperature variations are included in addition to the thermal cycles experienced due to the system's mission profile. This step

can also be implemented within MATLAB, using a function to describe each component's thermal mission profile, and perform failure rate calculations. This function based approach allows the thermal cycles extracted in Step 2 to be passed to the component's thermal mission profile function, before the thermal mission profile is passed to the failure rate function.

Considering fault-tolerant systems, if the thermal stresses seen by the component change in the post-fault state compared to the healthy state, then separate failure rates are calculated for the healthy and post-fault operating states according to the change in thermal cycles and average operating temperatures.

D. Step 4: Markov Modeling

Continuing within the MATLAB environment, Markov chain models are used to create reliability models of the power-electronic systems. Markov chains are characterized by the Markov property, that is, the system's future behavior depends only on the current state and the system is memoryless. Compared to combinatorial or fault tree reliability modeling methods, Markov chains are suited to modeling additional system states introduced by fault-tolerance or redundancy, as well as the process of repair. For example, a simple fault-tolerant system may have three states: the healthy state, the post-fault state, and the failure state. Both the healthy and post-fault states are considered "operational" states. The Markov model can be simulated as a state space system, in which the state variables are the probabilities over time of the system being in each state. The state matrix is obtained from the Markov transition rates, which for reliability modeling are a summation of failure or repair rates. See Section IV for a numerical example.

E. Step 5: Reliability Metrics

Reliability metrics can be directly calculated from the Markov transition matrices or from time-domain simulation of the Markov systems. The reliability modeling in this paper assumes an exponential failure distribution, in which failures occur randomly at a constant rate, corresponding to the flat "useful life" phase of the bathtub curve [24]. For a simple system with a constant failure rate λ, the probability that the system has failed (failure rate) is given by: $F(t) = 1 - e^{-\lambda t}$, and the probability that the system is operational (reliability rate) is given by: $R(t) = e^{-\lambda t}$. Then the Mean Time To Failure (MTTF) is defined as:

$$MTTF = \int_0^\infty R(t)\,dt = \frac{1}{\lambda} \tag{1}$$

Therefore, (1) can be applied to a Markov model with two states, an operational state and a failure state. If the Markov model has additional operational states, such as in a fault-tolerant or redundant system, the reliability rate is no longer exponential, and MTTF cannot be calculated as the reciprocal of a failure rate. Instead, the reliability rate can be found from time-domain simulation of the Markov state space model, which yields the state probabilities over time $\boldsymbol{x(t)}$. Then the reliability rate is found as the sum of the operational state probabilities. Further, MTTF can be obtained as the integral of the reliability rate, assuming the Markov model is simulated for a sufficiently large time such that the reliability rate has converged to approximately zero.

MTTF can also be calculated directly from the probability matrix P, which describes the probabilities of the system transitioning from each state to every other state [25]. Firstly, the Q matrix is derived from the P matrix by removing the rows and columns corresponding to the non-operational and absorbing states. Then MTTF is found as [26]:

$$M = [1 - Q] \tag{2}$$

$$N = [M]^{-1} \tag{3}$$

$$MTTF = \sum_{k=1}^{n} N_{1,k} \tag{4}$$

where the N matrix is of dimensions $n \times n$, and MTTF is calculated as the summation of the first row of the N matrix.

If the system is repairable, Mean Time Between Failures (MTBF) is used instead of MTTF. In general, MTBF is defined as:

$$MTBF = \frac{\text{operational time}}{\text{number of failures}}$$

As with MTTF, MTBF for a two state system with constant failure rate λ can be calculated as:

$$MTBF = \frac{1}{\lambda} \tag{5}$$

In systems with additional operational states, MTBF can no longer be calculated as the reciprocal of a constant failure rate. As time goes to infinity, the Markov model settles to a steady-state solution where the state probabilities are constant over time. A matrix V can be calculated as:

$$V = P^n \tag{6}$$

where n is a sufficiently large time that the Markov model has settled to the steady state. Then the rows of V are identical and are each the steady-state vector of state probabilities v. Then MTBF in the steady state can be calculated as:

$$\begin{aligned} MTBF &= \frac{\text{operational time}}{\text{number of failures}} \\ &= \frac{1}{\sum_{k=1}^{n} v_k \cdot \lambda_{kk}} \end{aligned} \tag{7}$$

where the Markov model has n states, and thus the dimensions of P and V are $n \times n$. v_k is the steady-state probability of state k and λ_{kk} is the sum of the failure rates from state k to all other states. If there are no failures from state k, then λ_{kk} is zero.

A similar metric Mean Time Between Repairs (MTBR) can also be defined as:

$$\begin{aligned} MTBR &= \frac{\text{operational time}}{\text{number of repairs}} \\ &= \frac{1}{\sum_{k=1}^{n} v_k \cdot \mu_{kk}} \end{aligned} \tag{8}$$

where μ_{kk} is the sum of repair rates from state k to all other states. If there are no repairs from state k, then μ_{kk} is zero. If all failures are repaired, then MTBR equals MTBF.

This article has been accepted for publication in a future issue of this journal, but has not been fully edited. Content may change prior to final publication. Citation information: DOI 10.1109/TIA.2022.3144620, IEEE Transactions on Industry Applications

In summary, this section has detailed the proposed reliability modeling framework. Step 1 uses PLECS and LTspice to obtain semiconductor device junction temperatures over the input mission profile (temperature profile). The next four steps are well integrated within the MATLAB/Simulink environment. The temperature profiles obtained in Step 1 are passed to the thermal cycle extraction algorithm in Step 2. In Step 3, the output thermal cycles are passed to functions for component thermal mission profiles (temperature variation over an entire year, as described in IEC 62380). These thermal mission profiles are then passed to functions for failure rate calculation along with other device and environmental parameters. In Step 4, Markov models are created and simulated, where the Markov transition rates are formed as the summation of the component failure rates calculated in Step 3. Finally, in Step 5, reliability metrics MTTF, MTBF, and MTBR can be calculated directly from the Markov models. However, the Markov models can also be simulated to yield graphical plots of system reliability rates or individual state probabilities over time.

III. Case Study: eVTOL UAV Propulsion System

A. Overview

The proposed reliability modeling framework will now be demonstrated through a case study of an eVTOL UAV. This section details the UAV parameters, the fault-tolerant techn-qiue applied to the UAV DC-AC inverters, and the mission profile flown by the UAV. Then Section IV walks through the reliability modeling framework to compare the UAV's reliability with and without fault tolerance or redundancy.

The vehicle's fully electric propulsion system has four PMSM drive units, each of which contains a three-phase DC-AC inverter. To concisely demonstrate the framework, the scope of the reliability modeling is limited to the inverter and its control. The effects of adding fault tolerance to the inverter are studied by comparing the fault-tolerant inverter to a baseline inverter with no fault tolerance. The inclusion of repairs is also considered. Therefore at the inverter level three 'levels' of fault-tolerance are studied: 'FT0' is the baseline inverter with no fault-tolerance; 'FT1' is the fault-tolerant inverter without repair; and 'FT2' is the fault-tolerant inverter with repair. Then the framework can be applied to a system with both fault tolerance and redundancy. Consider the FT0, FT1, and FT2 levels of inverter fault tolerance in tandem with two levels of redundancy at the propulsion system level: 'R0' being no redundancy, i.e., if one PMSM drive unit fails completely, so does the entire propulsion system; 'R1' being n-1 redundancy, i.e., the UAV with n = 4 drive units can still operate despite the loss of a single PMSM drive unit. This allows for fault-tolerant or redundant systems to be compared to a baseline non-fault-tolerant non-redundant propulsion system, based on quantitative reliability metrics.

From the reliability perspective, the addition of the fault tolerance has both positive and negative effects. Additional components lead to a more complex inverter circuit which suffers more failures than the baseline system. However, this is offset by the addition of the post-fault operating state, which allows the system to continue operating following a failure. In a realistic operational scenario, the aircraft would be grounded and repaired prior to being returned to service (FT2), dramatically improving reliability. Alternatively, in the FT1 case with no repairs, the system would be left in normal service despite entering the post-fault operating state. Whilst not a realistic use case in aviation, this may be acceptable in other applications and is thus included for completeness.

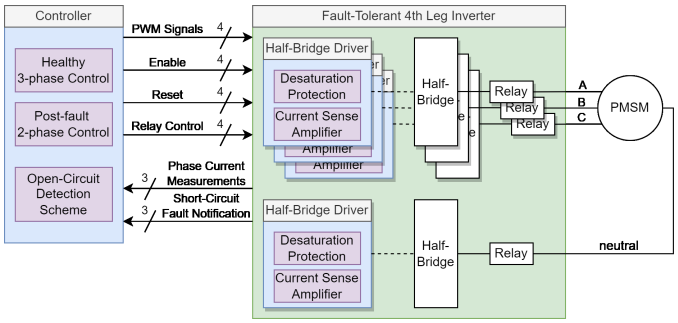

Fig. 3. Fault-tolerant 4th leg inverter topology, with open-circuit detection in the controller and short-circuit detection provided by gate driver desaturation protection. Relays allow for inverter reconfiguration following a fault.

B. Fault-tolerant System Design

The PMSM drive's three-phase inverter is designed to be fault tolerant to a single switch open- or short-circuit failure. In this case study, a 4th inverter leg connected to the motor neutral [21], [27] is used to add fault tolerance to the inverter, though other topologies and controls can also be chosen. The design of a fault-tolerant 4th leg inverter drive for aviation applications is shown in Fig. 3, and was detailed in the authors' previous work [1].

Following a fault, the faulted phase is isolated from the rest of the drive, and the 4th inverter leg is connected to the motor neutral point, allowing the system to continue operating with a post-fault two-phase control scheme. Under post-fault control, the currents are significantly higher for the same load condition. The two un-faulted phase currents are phase shifted and $\sqrt{3}$ times in magnitude compared to healthy operation. Additionally, the neutral current flowing through the 4th inverter leg is 3 times the healthy phase current magnitude. Therefore, flying the same mission profile in the post-fault operating state leads to higher currents, higher temperature swings, and accelerated device aging. The proposed framework includes these effects in the reliability modeling of the system. By simulating the system over the same mission profile in healthy and post-fault operating states, different failure rates for healthy and post-fault states are calculated according to the change in device thermal behaviors.

C. eVTOL UAV Parameters and Mission Profile

The case study eVTOL UAV uses a design from the authors' previous work [28]. The eVTOL aircraft mass is estimated as shown in Table III in order to ensure the mission profile uses realistic thrust values. The simulated propulsion unit uses T-Motor G28x9.2 propeller parameters, T-Motor U10II KV100

This article has been accepted for publication in a future issue of this journal, but has not been fully edited. Content may change prior to final publication. Citation information: DOI 10.1109/TIA.2022.3144620, IEEE Transactions on Industry Applications

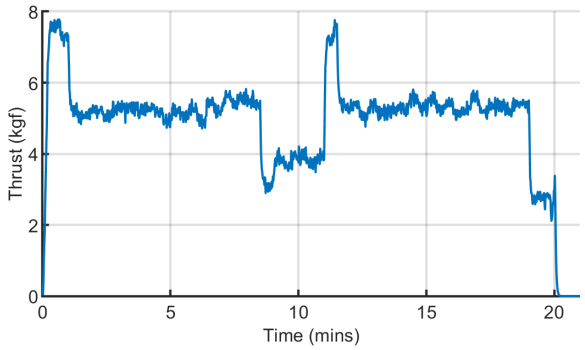

Fig. 4. Mission profile showing average thrust per propeller over a typical 20-minute flight.

motor parameters, and an inverter with Infineon IPB073N15N5 D2PAK MOSFETs. Each phase of the inverter has a single upper and lower MOSFET. However, the 4th inverter leg has two MOSFETs in parallel (four total) in order to handle the large neutral current during the post-fault operating state. The increased failure rate due to the extra MOSFETs is included in the reliability modeling of the fault-tolerant inverters.

Fig. 4 shows the mission profile of the eVTOL UAV as the average thrust per propeller over a 20-minute flight. The mission profile assumes that the required climbing thrust is twice the aircraft mass, cruising thrust is 1.4 times, hover thrust is 1 times, and descending thrust is 0.8 times. The thrust per propeller is then calculated considering the total aircraft mass from Table III and the number of propellers. The UAV performs the same mission profile in the healthy and post-fault operating states. Whilst the flight mission profile remains the same in the post-fault operating state, the MOSFETs see different current magnitudes compared to the healthy state. The remaining phase leg MOSFETs see $\sqrt{3}$ times higher currents, and the 4th leg MOSFETs see 1.5 times higher current (3 times total split between two MOSFETs in parallel).

IV. Application of the Reliability Modeling Framework

A. Step 1: Multiphysics Modeling

The modeling includes mechanical, electrical, and thermal aspects. PLECS is used as the primary simulation environment,

TABLE III
eVTOL UAV Mass Estimation

Component	Data Source for Mass Calculation	Mass (kg)
Propellers	T-Motor G28x9.2, specified mass.	0.392
Motors	T-Motor U10II KV100, specified mass.	1.660
Inverters	T-Motor Alpha 80A HV, specified mass.	0.440
Battery Pack	Tattu 10000mAh 6s 25C Li-Po, Wh/kg.	5.543
DC-DC Converter	US Drive EETT Roadmap, PE 2020 target power density, kW/kg.	1.417
Frame + Wiring	Estimated, 20% of 15kg target mass.	3.000
Aux Electronics	Estimated	0.200
Payload	Available mass before 15kg target.	2.348
	Total	15.00

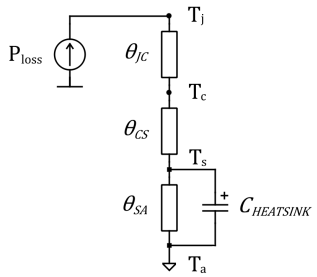

Fig. 5. MOSFET thermal model used within the PLECS simulation.

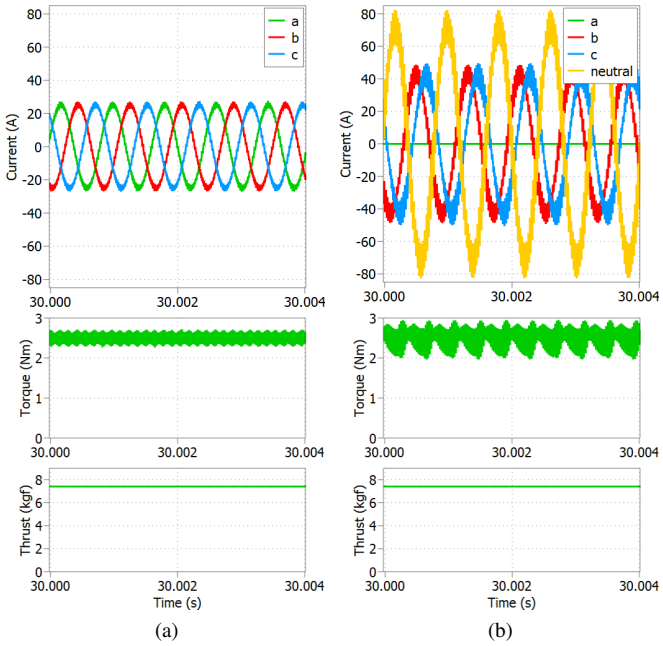

(a) (b)

Fig. 6. (a) Healthy operating state PMSM currents, PMSM torque, and propeller thrust at t = 30 s of the mission profile in Fig. 4. (b) Same variables for the post-fault operating state.

in which the electrical system is simulated over the mission profile of Fig. 4. The authors' previous experimental testing of a T-motor G28x9.2 propeller with a T-motor U10II motor provides real torque and thrust values over the speed range of the motor [28]. This data forms a lookup table based model of the mechanical system in PLECS. For a given mission profile thrust in Fig. 4, the corresponding motor speed at which this thrust is produced is set as the commanded speed in the controller. Another lookup table sets the motor load torque according to the measured motor speed. The simulation of the electrical system is dynamic, including control system transient behavior and PWM switching. Separately, the SPICE model of the IPB073N15N5 MOSFET is used in LTspice to generate the conduction and switching loss lookup table data for the MOSFETs. Fig. 5 shows the lumped parameter thermal model for each MOSFET implemented in PLECS. P_{loss} is the combined conduction and switching losses for a single MOSFET. θ_{JC} is a junction-case thermal resistance of 0.7 K/W, θ_{CS} is a case-sink thermal resistance of 0.87 K/W, θ_{SA} is a sink-ambient thermal resistance of 11 K/W, and $C_{HEATSINK}$ is a thermal capacitance of 1.5 J/K. T_J, T_C, T_S,

This article has been accepted for publication in a future issue of this journal, but has not been fully edited. Content may change prior to final publication. Citation information: DOI 10.1109/TIA.2022.3144620, IEEE Transactions on Industry Applications

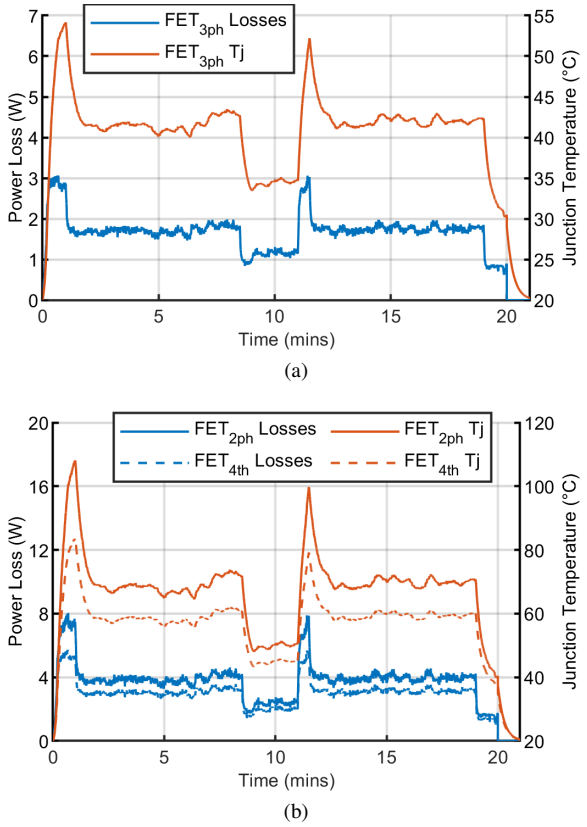

Fig. 7. Inverter MOSFET power losses and temperatures over the mission profile of Fig. 4. (a) During healthy operation. (b) During post-fault operation.

and T_A are the junction, case, sink, and ambient temperatures, respectively. θ_{JC} is provided by the MOSFET manufacturer, whilst the other parameters are estimated for an appropriately sized heatsink with low airflow convective cooling.

Two PLECS models are constructed, one for the healthy operation state, and the other for the post-fault operation state, based on the inverter circuitry and control discussed in Section III. This allows the change in device currents and temperatures due to the post-fault operation state to be fully captured. Fig. 6 shows the change in device currents from the healthy to post-fault operating states for a given load condition. For example, at t = 30 s in the mission profile, the required thrust is 7.41 kgf, which corresponds to a PMSM speed of 3505 rpm and a load torque of 2.50 Nm. In the healthy state the phase currents are 17.7 A rms. In the post-fault operating state for the same load condition, the 'b' and 'c' phase currents are now 30.2 A rms ($\sim \sqrt{3}$ times) and the neutral current is 51.2 A rms (~ 3 times). Due to the higher currents in the post-fault operating state, the phase MOSFETs experience increased losses and higher temperatures throughout the mission profile. Therefore, although the UAV performs the same mission profile in the post-fault operating state, the failure rate of components such as the inverter MOSFETs will be increased.

Fig. 7 shows MOSFET power losses and junction temperatures during (a) healthy operation and (b) post-fault operation. In healthy operation, all phase MOSFETs (denoted FET_{3ph}) see the same load currents and temperature changes. However, in post-fault operation, the two remaining phase leg MOSFETs see different currents and temperatures compared to the 4th leg MOSFETs (denoted FET_{2ph} and FET_{4th} respectively).

TABLE IV
EXTRACTED MOSFET THERMAL CYCLES

MOSFETs	Extracted Thermal Cycles over Mission Profile ($^\circ C$)						
FET_{3ph}	34.2	3.50	18.8	-	-	-	-
FET_{2ph}	88.1	3.35	3.37	9.34	51.7	4.86	4.65
FET_{4th}	63.8	6.67	35.9	3.53	3.37	-	-

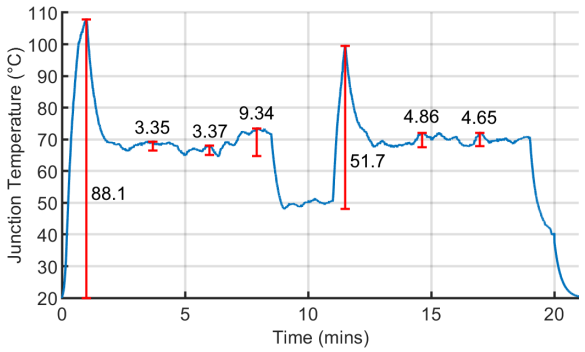

Fig. 8. Junction temperature for FET_{2ph} with extracted thermal cycles.

B. Step 2: Thermal Cycle Extraction

The MOSFET junction temperatures from Fig. 7 are passed to the MATLAB thermal cycle extraction algorithm, as described in Section II. No preprocessing of the junction temperature profile is required, and the thermal cycle extraction process requires no manual effort. Table IV shows the extracted thermal cycles for each group of MOSFETs. To illustrate this step, for example for the data in the second row of Table IV, Fig. 8 shows the extracted thermal cycles for FET_{2ph} overlaid on the FET_{2ph} junction temperatures from Fig. 7(b).

C. Step 3: Failure Rate Calculation

Failure rate calculation in IEC 62380 requires the use of year-long thermal mission profiles. The thermal mission profile includes the thermal cycles obtained via Steps 1 and 2, the average operating temperatures obtained in Step 1, and any environmental variations. Note that the thermal mission profile is distinct from the temperature profile, where the former is defined in IEC 62380 and captures component temperature variations over an entire year, whilst the latter is the component's temperature over the mission profile, obtained in Step 1. The case study UAV performs 10 flights per day for 351 days in one year. Therefore, the MOSFETs undergo each cycle in Table IV 3510 times per year. Since the thermal mission profiles are different from healthy to post-fault operation, the calculated failure rates for each group of MOSFETs will be different.

The increased average operating temperatures of the MOSFETs increase the Arrhenius relation acceleration factor which is applied to the MOSFET die base failure rate. The increased magnitudes and number of thermal cycles in Table IV will

This article has been accepted for publication in a future issue of this journal, but has not been fully edited. Content may change prior to final publication. Citation information: DOI 10.1109/TIA.2022.3144620, IEEE Transactions on Industry Applications

TABLE V
CALCULATED COMPONENT FAILURE RATES

Component	failures/hour	Component	failures/hour
$\lambda_{FET_{3ph}}$	1.84×10^{-7}	λ_{buck}	6.99×10^{-8}
$\lambda_{FET_{2ph}}$	3.83×10^{-7}	$\lambda_{CON_{MCU}}$	2.12×10^{-7}
$\lambda_{FET_{4th}}$	2.86×10^{-7}	$\lambda_{CON_{DC}}$	1.50×10^{-7}
$\lambda_{Rs_{3ph}}$	1.71×10^{-10}	$\lambda_{CON_{MOTOR}}$	1.06×10^{-7}
$\lambda_{Rs_{2ph}}$	1.78×10^{-10}	$\lambda_{RELAY_{SC}}$	2.39×10^{-8}
$\lambda_{C_{bus}}$	1.74×10^{-8}	$\lambda_{RELAY_{OC}}$	9.54×10^{-8}

change the Coffin-Mason based acceleration factor applied to the MOSFET package base failure rate. The die failure rate is also modified by the charge factor, which varies with the ratio of the drain-source voltage stress and rating, and the ratio of the gate-source voltage stress and rating. The full failure rate equations used for each component are available in IEC 62380 [11], and are not reproduced here due to copyright. Besides, the use of the equations is straightforward once the operating temperatures and thermal cycles have been obtained via Steps 1 and 2 of the proposed framework. Table V shows the calculated individual component failure rates for the inverter system. Note the different failure rates for the MOSFETs in the healthy operating state, $\lambda_{FET_{3ph}}$ and the post-fault operating state, $\lambda_{FET_{2ph}}$ and $\lambda_{FET_{4th}}$.

Since other components in the circuit see lesser temperature variations, their failure rates can be calculated without consideration of thermal cycles. Failure rates for the current sense resistor, DC link capacitor, connectors, relays, and gate drive power supply are also calculated. The failures of integrated circuit components such as the MCU and gate drivers are assumed to be negligible. In the next step, the calculated failure rates are used directly in the Markov transition matrices to form the system reliability models.

D. Step 4: Markov Modeling

Firstly, reliability models of the FT0, FT1, and FT2 inverter systems are created. Fig. 9(a) shows the FT0 Markov model: There is an operational state S_1 and a failure state S_2. Initially, the probability of the system being in the operational state is 1 and in the failure state is 0. However, over time the probability that the system will be in the failure state increases exponentially according to $P(S_2) = 1 - e^{-\lambda_{fatal\_A}t}$, where λ_{fatal_A} is a summation of failure rates as shown in Table VI.

Fig. 9(b) shows the FT1 and FT2 Markov models, where the inclusion of repairs in FT2 adds the dashed arrow with

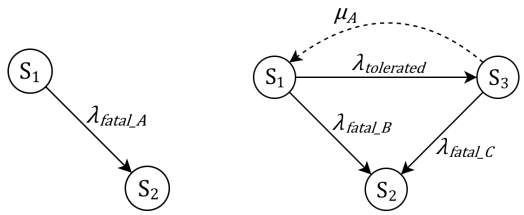

Fig. 9. Markov models of the inverter systems under study. (a) Non fault-tolerant three-phase inverter (FT0). (b) Fault-tolerant 4th leg inverter, without repairs (FT1), and with repairs (FT2). The inclusion of repairs for the FT2 case is shown by the dashed arrow.

transition rate μ_A. S_1 is still the initial operational state, and S_2 is the failure state representing a catastrophic failure. However, the fault tolerance introduces an additional operational state S_3, corresponding to post-fault operation following a tolerated MOSFET failure. Since the 4th leg inverter is only fault tolerant to MOSFET failures, the inverter can transition to either S_2 or S_3 depending on which component fails, according to transition rates λ_{fatal_B} and $\lambda_{tolerated}$ respectively. Repair in this context means that when the inverter enters post-fault operation (S_3), it can be returned to healthy three-phase (S_1) if the failed components are physically replaced. This creates the transition rate μ_A for the FT2 system, which is the number of repairs per hour. If the system is in S_3, it will fail catastrophically if any further components fail. This leads to the transition rate λ_{fatal_C} from S_3 to the failure state S_2. Table VI shows the calculation and values of all Markov transition rates.

Secondly, reliability models of the eVTOL UAV propulsion system are created, considering RT0 and RT1 cases in tandem with FT0, FT1, or FT2. This allows the study of how fault tolerance in the inverter subsystem affects the overall reliability of the aircraft propulsion system. The eVTOL UAV has four propellers, four motors, and four inverters. To simplify the analysis, this study only includes failures in the motor drives in the propulsion system reliability models. In practice, propeller, motor, wiring, and battery failures should also be included. Whilst less realistic, the aim of this analysis is to demonstrate the use of the reliability modeling framework to study fault tolerance in tandem with higher level redundancy.

Fig. 10 shows the Markov models of the six possible combinations of fault tolerance and redundancy. Note that the R0 and R1 cases share the same figures for conciseness, however, their respective Markov models are different. For R0,

TABLE VI
MARKOV MODEL TRANSITION RATES

Transition Rate	failures/hour or repairs/hour	Calculation
λ_{fatal_A}	1.87×10^{-6}	$6\lambda_{FET_{3ph}} + 3\lambda_{Rs_{3ph}} + \lambda_{CON_{MCU}} + \lambda_{CON_{DC}} + 3\lambda_{CON_{MOTOR}} + \lambda_{C_{bus}} + \lambda_{buck}$
λ_{fatal_B}	5.21×10^{-7}	$\lambda_{CON_{MCU}} + \lambda_{CON_{DC}} + \lambda_{C_{bus}} + \lambda_{buck} + 3\lambda_{RELAY_{SC}}$
λ_{fatal_C}	3.71×10^{-6}	$\lambda_{fatal\_B} + 4\lambda_{FET_{2ph}} + 4\lambda_{FET_{4th}} + 2\lambda_{Rs_{2ph}} + 3\lambda_{CON_{MOTOR}} + 3\lambda_{RELAY_{OC}}$
$\lambda_{tolerated}$	1.71×10^{-6}	$6\lambda_{FET_{3ph}} + 3\lambda_{Rs_{3ph}} + 3\lambda_{CON_{MOTOR}} + 3\lambda_{RELAY_{OC}}$
μ_A, μ_B	0.1	assumed 10 hour repair time

This article has been accepted for publication in a future issue of this journal, but has not been fully edited. Content may change prior to final publication. Citation information: DOI 10.1109/TIA.2022.3144620, IEEE Transactions on Industry Applications

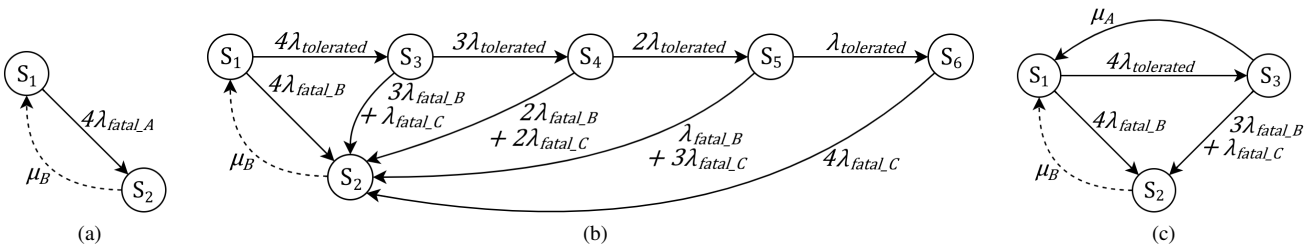

Fig. 10. Markov models of the eVTOL UAV propulsion systems. (a) Non-redundant or n-1 redundant propulsion system with non fault-tolerant inverters (FT0 + R0 or R1). (b) Non-redundant or n-1 redundant propulsion system with fault-tolerant inverters, which are not repaired until they fail catastrophically (FT1 + R0 or R1). (c) Non-redundant or n-1 redundant propulsion system with fault-tolerant inverters, which are repaired as soon as they suffer a tolerated or fatal failure (FT2 + R0 or R1).

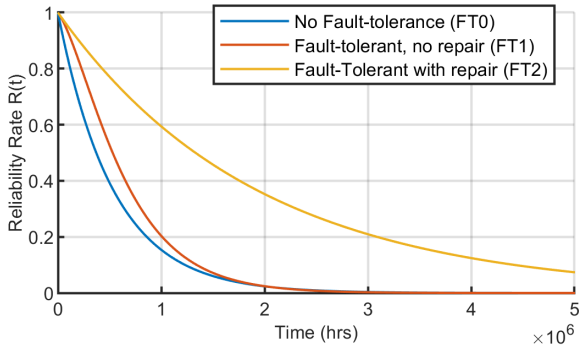

Fig. 11. Reliability rates of FT0, FT1, and FT2 fault tolerance scenarios.

S_2 is a failure state, whereas for R1, S_2 is an operational state corresponding to propulsion with 3 out of 4 PMSM drive units operational. For R1, repairs are always included, i.e., once the aircraft loses a PMSM drive unit and enters state S_2, it will be promptly repaired before returning to service with four PMSM drive units in healthy condition (S_1), according to repair rate μ_B.

E. Step 5: Reliability Metrics

Simulating the inverter Markov models of Fig. 9 yields a reliability rate $R(t)$ for each fault tolerance scenario as shown in Fig. 11. Here the reliability rate is the probability over time of the system being in an operational state, including healthy three-phase operation (S_1) and post-fault two-phase operation (S_3) if applicable.

The MTTF metrics for each inverter system are shown in Table VII. As expected, the fault-tolerant 4th leg inverter increases the MTTF compared to a baseline inverter with no fault tolerance (FT0). Without repairs (FT1), the increase in MTTF is relatively small. This is explained by multiple factors. Firstly, the inverter is only fault tolerant to a single MOSFET failure. Therefore, it will still fail completely if any other component fails or a second MOSFET failure occurs. Secondly, the failure rates of the fault-tolerant inverter are higher than in the baseline inverter due to the increased complexity. However, since the first MOSFET failure is now tolerated, an increase in MTTF is still achieved due to continuing operation in the post-fault state. When repairs are included (FT2), the MTTF increases dramatically. In practical terms, when the inverter suffers a MOSFET failure and transitions to the post-fault

TABLE VII
INVERTER MEAN TIME TO FAILURE

Inverter System	Mean Time to Failure (MTTF)
'FT0' No Fault tolerance (baseline)	5.35×10^5 hrs
'FT1' Fault tolerance, no repairs	6.55×10^5 hrs
'FT2' Fault tolerance, repairs	19.2×10^5 hrs

operating state (S_3), the UAV is removed from service until the inverter is repaired. In the Markov model this is reflected by the repair rate μ_A being several orders of magnitude greater than the failure rates $\lambda_{tolerated}$ and λ_{fatal_C}.

Simulation of the propulsion system Markov models (Fig. 10) generates the reliability rates shown in Fig. 12. Note that when there is n-1 redundancy with repair in the propulsion system (R1), the system never fails completely. Therefore, the reliability rate for all three R1 systems is constant at one and their MTTF is theoretically infinite. Considering the R0 systems, using fault-tolerant inverters (R0 + FT1 or FT2) improves the reliability rate. As before, the reliability improvement is better quantified by the reliability metrics shown in Table VIII. If there is no redundancy at the system level (R0), then the propulsion system and therefore the entire aircraft is vulnerable to catastrophic failure, even if the inverter is fault tolerant. This is because even in the fault-tolerant inverter topologies there are still single points of failures. Considering the R0 cases, a fault-tolerant inverter (FT1 or FT2) offers a considerable improvement in MTTF. If the propulsion system is designed to have n-1 redundancy at the

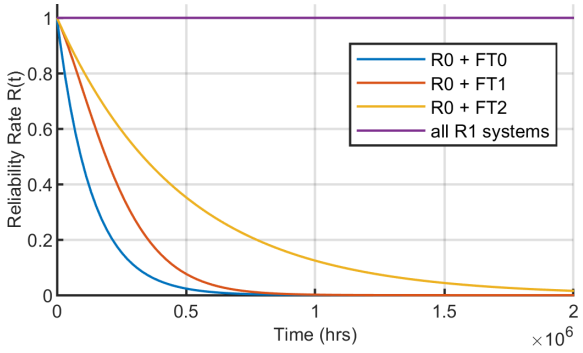

Fig. 12. Reliability rates of the eVTOL UAV propulsion system considering the possible combinations of redundancy and fault tolerance.

TABLE VIII
RELIABILITY METRICS OF A PROPULSION SYSTEM WITH FOUR DRIVE UNITS

System Level Redundancy	Inverter System Fault-Tolerance	Mean Time To Failure (MTTF)	Mean Time Between Failures (MTBF)	Mean Time Between Repairs (MTBR)
'R0' No Redundancy	'FT0' No Fault tolerance (baseline)	1.34×10^5 hrs	-	-
'R0' No Redundancy	'FT1' Fault tolerance, no repairs	2.27×10^5 hrs	-	-
'R0' No Redundancy	'FT2' Fault tolerance, repairs	4.80×10^5 hrs	-	-
'R1' n-1 Redundancy, repairs	'FT0' No Fault tolerance (baseline)	-	1.34×10^5 hrs	1.34×10^5 hrs
'R1' n-1 Redundancy, repairs	'FT1' Fault tolerance, no repairs	-	1.00×10^5 hrs	2.27×10^5 hrs
'R1' n-1 Redundancy, repairs	'FT2' Fault tolerance, repairs	-	1.12×10^5 hrs	1.12×10^5 hrs

system level (R1), then fault tolerance has no effect on MTTF. Note that in the 5th row (R1 + FT1), the drive unit is not repaired after entering the post-fault operating state, but is repaired after the drive unit fails completely. This is not a realistic operational scenario, but it is considered here for completeness.

For the R1 cases we consider the MTBF and MTBR metrics. For R1 with FT1 or FT2, MTBF is reduced (worse) compared to R1 with FT0, due to the fault tolerance increasing the failure rates of the inverter. However, this does not necessarily mean that the propulsion system is less safe. On the contrary, most of the fault-tolerant inverter failures will be tolerated failures, in which the inverter transitions to the post-fault operating state rather than failing completely. This is supported by comparing the S_1 to S_2 transition rates in Fig. 10. When fault tolerance is added, the transition rate is reduced from $7.48\text{x}10^{-6}$ to $2.08\text{x}10^{-6}$ failures/hour. Therefore, although failures are more frequent in the systems with fault tolerance, the propulsion system visits the redundant state S_2 (in which 3 out of 4 drive units are operational) less frequently compared to the redundant system with no fault tolerance.

V. CONCLUSION

This paper proposes a mission profile based reliability modeling framework for fault-tolerant power electronic systems, with an emphasis on aviation propulsion but applicable to a variety of power-electronic applications. In contrast to existing reliability studies of fault-tolerant systems, failure rates are calculated considering the mission profile of the system and the resultant thermal stresses on the semiconductor devices. The hierarchical framework leverages multiphysics modeling to simulate semiconductor device junction temperatures over the system mission profile, and the thermal cycles are automatically identified by a MATLAB algorithm as shown in the Appendix. Failure rates are calculated using IEC 62380 with inclusion of the thermal stresses, followed by Markov chain reliability modeling under various fault-tolerant or redundant system scenarios.

Compared to other mission profile based reliability modeling techniques, this paper includes numerous provisions for the reliability analysis of fault-tolerant or redundant systems, and a case study of an eVTOL UAV propulsion system demonstrates its efficacy. Firstly, multiphysics simulation captures the change in device temperatures in the post-fault operating state compared to healthy operation, and pre- and post-fault failure rates are calculated for the semiconductor devices according to the change in thermal stress via physics based acceleration factors. Secondly, Markov models facilitate the multiple system states for the fault-tolerant or redundant systems, and accommodate state-dependent failure rates. Lastly, the framework details the calculation of MTBF and MTBR metrics for a repairable fault-tolerant or redundant system. Accordingly, the reliability modeling framework was successfully used to compare between eVTOL UAV propulsion systems with fault tolerance, redundancy, or both, and a baseline system with no fault tolerance or redundancy.

This reliability modeling framework bridges the gap between existing mission profile based techniques which use a physics-of-failure approach and reliability studies which employ empirical data sets. The proposed framework enables the inclusion of thermal stresses due to the system mission profile in the failure rate calculation. Compared to a PoF approach, detailed knowledge of component structure and failure modes is not required, and thus the framework can be rapidly applied to any power electronics based system, so long as the system can be simulated over its typical mission profile and a SPICE model is available for the switching devices. Therefore, the framework is well-suited to the preliminary design stage, where it enables a reliability comparison between multiple candidate systems with consideration of the system mission profile and associated thermal cycling, and fault tolerant or redundant system options.

APPENDIX
MATLAB FUNCTION FOR THERMAL CYCLE EXTRACTION

```
function[cycles] = ExtractCycles(maxima,minima)
%1st cycle is highest maxima minus mean of 1st/last minima
cycles_id(1) = find(maxima==max(maxima));
minima_mean = 0.5*(minima(1) + minima(length(minima)));
cycles(1) = max(maxima) - minima_mean;
maxima(cycles_id(1)) = 0; %remove maxima from search
for i = 2:1:(length(maxima)) %for remaining maxima
    cycles_id(i) = find(maxima==max(maxima));%move to next
    %if current maxima is to left of maxima
    if cycles_id(i) < cycles_id(1)
        %use minima to right
        cycles(i) = max(maxima) - minima(cycles_id(i)+1);
    else
        %use minima to left
        cycles(i) = max(maxima) - minima(cycles_id(i));
    end
    maxima(cycles_id(i)) = 0;%remove maxima from search
end
%order cycles by order of input maxima
C = sortrows([cycles_id;cycles]')';
cycles = C(2,:);
end
```

REFERENCES

[1] A. P. Thurlbeck and Y. Cao, "Fully integrated fault-tolerance for PMSMs in aviation applications," in *Proc. IEEE Energy Conversion Congr. and Expo. (ECCE)*, 2020, pp. 4916–4922.

[2] J. A. Rosero, J. A. Ortega, E. Aldabas, and L. Romeral, "Moving towards a more electric aircraft," *IEEE Aerospace and Electronic Systems Magazine*, vol. 22, no. 3, pp. 3–9, 2007.

[3] P. Wheeler and S. Bozhko, "The more electric aircraft: Technology and challenges." *IEEE Electrification Magazine*, vol. 2, no. 4, pp. 6–12, 2014.

[4] P. Wheeler, "Technology for the more and all electric aircraft of the future," in *Proc. IEEE Int. Conf. on Automatica (ICA-ACCA)*, 2016, pp. 1–5.

[5] R. D. Rosario, "A future with hybrid electric propulsion systems: A nasa perspective," in *Proc. Turbine Engine Technol. Symp. Strategic Vis. Workshop*, 2014, pp. 1–21.

[6] N. K. Borer, M. D. Patterson, J. K. Viken, M. D. Moore, J. Bevirt, A. M. Stoll, and A. R. Gibson, "Design and performance of the NASA SCEPTOR distributed electric propulsion flight demonstrator," in *Proc. 16th AIAA Aviation Technology, Integration, and Operations Conf.*, 2016.

[7] M. Pecht and A. Dasgupta, "Physics-of-failure: an approach to reliable product development," in *IEEE 1995 Int. Integrated Reliability Workshop. Final Report*, Oct. 1995, pp. 1–4.

[8] H. Wang, M. Liserre, F. Blaabjerg, P. de Place Rimmen, J. B. Jacobsen, T. Kvisgaard, and J. Landkildehus, "Transitioning to Physics-of-Failure as a Reliability Driver in Power Electronics," *IEEE Trans. Emerg. Sel. Topics Power Electron.*, vol. 2, no. 1, pp. 97–114, Mar. 2014.

[9] H. Oh, B. Han, P. McCluskey, C. Han, and B. D. Youn, "Physics-of-Failure, Condition Monitoring, and Prognostics of Insulated Gate Bipolar Transistor Modules: A Review," *IEEE Trans. Power Electron.*, vol. 30, no. 5, pp. 2413–2426, May 2015.

[10] *Military Handbook: Reliability prediction of electronic equipment*, MIL-HDBK-2 1 7F, 1991.

[11] *Reliability data handbook - Universal model for reliability prediction of electronics components, PCBs and equipment*, IEC TR 62380:2004, 2004. [Online]. Available: https://webstore.iec.ch/publication/6946

[12] *FIDES Reliability Methodology for Electronic Systems*, Fides Guide 2009 Edition A, 2009. [Online]. Available: https://www.fides-reliability.org/en

[13] H. Wang, K. Ma, and F. Blaabjerg, "Design for reliability of power electronic systems," in *IECON 2012 - 38th Annual Conf. on IEEE Industrial Electronics Society*, Oct. 2012, pp. 33–44.

[14] M. Musallam, C. Yin, C. Bailey, and M. Johnson, "Mission Profile-Based Reliability Design and Real-Time Life Consumption Estimation in Power Electronics," *IEEE Trans. Power Electron.*, vol. 30, no. 5, pp. 2601–2613, May 2015.

[15] D. Hirschmann, D. Tissen, S. Schroder, and R. W. De Doncker, "Reliability Prediction for Inverters in Hybrid Electrical Vehicles," *IEEE Trans. Power Electron.*, vol. 22, no. 6, pp. 2511–2517, Nov. 2007.

[16] G. El Murr, A. Griffo, J. Wang, Z. Q. Zhu, and B. Mecrow, "Reliability assessment of fault tolerant permanent magnet AC drives," in *Proc. Annu. Conf. of the IEEE Industrial Electronics Society (IECON)*, 2015, pp. 2777–2782.

[17] J. Xu, H. Guo, X. Kuang, and T. Zhou, "Reliability analysis approach to fault tolerant permanent magnet synchronous motor system," in *Proc. IEEE Vehicle Power and Propulsion Conf. (VPPC)*, 2016, pp. 1–5.

[18] N. Brinzei and B. Nahid-Mobarakeh, "Reliability assessment of adjustable speed drives using state markov models," in *Proc. IEEE Industry Application Society Annu. Meeting*, 2014, pp. 1–8.

[19] R. N. Argile, B. C. Meerow, D. J. Atkinson, A. G. Jack, and P. Sangha, "Reliability analysis of fault tolerant drive topologies," in *Proc. 4th IET Conf. on Power Electronics, Machines and Drives*, 2008, pp. 11–15.

[20] Y. Song and B. Wang, "Analysis and experimental verification of a fault-tolerant hev powertrain," *IEEE Trans. Power Electron.*, vol. 28, no. 12, pp. 5854–5864, 2013.

[21] S. Bolognani, M. Zordan, and M. Zigliotto, "Experimental fault-tolerant control of a PMSM drive," *IEEE Trans. Ind. Electron.*, vol. 47, no. 5, pp. 1134–1141, 2000.

[22] D. Graovac and M. Purschel, *MOSFET Power Losses Calculation Using the Data-Sheet Parameters*, Infineon Application Note, 2006.

[23] *Standard Practices for Cycle Counting in Fatigue Analysis*, ASTM E1049 - 85(2017), 2017. [Online]. Available: https://www.astm.org/Standards/E1049.htm

[24] G. Klutke, P. Kiessler, and M. Wortman, "A critical look at the bathtub curve," *IEEE Trans. Reliab.*, vol. 52, no. 1, pp. 125–129, 2003.

[25] A. M. Bazzi, A. Dominguez-Garcia, and P. T. Krein, "Markov Reliability Modeling for Induction Motor Drives Under Field-Oriented Control," *IEEE Trans. Power Electron.*, vol. 27, no. 2, pp. 534–546, Feb. 2012.

[26] J. Börcsök, E. Ugljesa, and D. Machmur, "Calculation of MTTF values with markov models for safety instrumented systems," in *Proc. 7th Int. Conf. on Applied Computer Science*, 2007, pp. 30–35.

[27] O. Wallmark, L. Harnefors, and O. Carlson, "Control algorithms for a fault-tolerant PMSM drive," *IEEE Trans. Ind. Electron.*, vol. 54, no. 4, pp. 1973–1980, 2007.

[28] A. P. Thurlbeck and Y. Cao, "Analysis and modeling of uav power system architectures," in *Proc. IEEE Transportation Electrification Conf. and Expo (ITEC)*, 2019, pp. 1–8.

Alastair P. Thurlbeck (Graduate Student Member, IEEE) received the M.Eng. degree (first class honors) in electronics and electrical engineering from the University of Glasgow, Glasgow, UK, in 2018.

Mr. Thurlbeck is currently a Ph.D. candidate at Oregon State University, Corvallis, OR, USA. He has been a Research Scientist Intern at Amazon Prime Air in Seattle, WA, USA; a Project Assistant with the University of Glasgow; a Hardware Intern with Curtis Instruments in Livermore, CA, USA; and a Summer Intern with Arqiva in Winchester, UK. His research interests include power electronics, motor drives, energy conversion, fault tolerance, and reliability.

Mr. Thurlbeck received the IEEE ITEC Conference Student Award in 2019. He was awarded the Gilbert Cook Prize in 2018, the William Dawson Bursary in 2015 and the Reid Foster prize in 2014 by the University of Glasgow. He was a recipient of the Diamond Jubilee Scholarship throughout his MEng degree, awarded by the Institute of Engineering and Technology (IET) in 2013.

Yue Cao (Member, IEEE) received the B.S. degree (Hons.) in electrical engineering with a second major in mathematics from the University of Tennessee, Knoxville, TN, USA, in 2011, and the M.S. and Ph.D. degrees in electrical engineering from the University of Illinois at Urbana–Champaign (UIUC), Champaign, IL, USA, in 2013 and 2017, respectively.

Dr. Cao is currently an Assistant Professor with the Energy Systems Group at Oregon State University (OSU), Corvallis, OR, USA. Before joining OSU, he was a Research Scientist with the Propulsions Team at Amazon Prime Air in Seattle, WA, USA. He was a Power Electronics Engineer Intern with Special Projects Group at Apple Inc., Cupertino, CA, USA; Halliburton Company, Houston, TX, USA; Flanders Electric, Evansville, IN, USA; and Oak Ridge National Laboratory, TN, USA. He was a Sundaram Seshu Fellow in 2016 at UIUC, where he was a James M. Henderson Fellow in 2012. His research interests include power electronics, motor drives, and energy storage with applications in renewable energy integration and transportation electrification.

Dr. Cao was a national finalist of the USA Mathematical Olympiad (USAMO) in 2006 and 2007. He received the Myron Zucker Award from the IEEE Industry Applications Society (IAS) in 2010. He won the Oregon State Learning Innovation Award for transformative education in 2020. He is a recipient of the 2022 NSF CAREER award. Dr. Cao is currently the Special Sessions Chair of the 2022 IEEE Energy Conversion Congress Expo (ECCE) and was the Tutorials Chair of 2021 ECCE. He is a board member and Award Chair of IEEE Power Electronics Society (PELS) TC11 – Aerospace Power. In 2020, he helped establish an IEEE PELS Chapter at OSU. He is currently an Associate Editor for IEEE Transactions on Transportation Electrification and an Associate Editor for IEEE Transactions on Industry Applications.